Journal of Materials Chemistry C

ROYAL SOCIETY OF CHEMISTRY

PAPER

View Article Online
View Journal | View Issue

Cite this: J. Mater. Chem. C, 2025, 13, 6922

Low-bandgap oligothiophene-naphthalimide oligomeric semiconductors for thermoelectric applications†

Matías J. Alonso-Navarro, ‡[ab] Osnat Zapata-Arteaga, ‡[c] Sergi Riera-Galindo, [c] Jiali Guo, [c] Aleksandr-Peredeventsv, [c] Edgar Gutiérrez-Fernández, [d] Juan Sebastián Reparaz, [c] Mar Ramos, [b] Christian Müller, [e] Jaime Martín, [d] Marta Mas-Torrent, [c] José L. Segura *[a] and Mariano Campoy-Quiles *[c]

State-of-the-art p-type organic conjugated polymers are mostly thiophene-based semiconductors. Still, novel chemical design and a fresh perspective on different polymer backbones could pave the way for new high-performing materials and a deep understanding of donor–acceptor conjugated assemblies. Herein we designed and synthesized two novel electroactive oligomeric materials based on a donor terthiophene unit endowed with a strong electron-withdrawing naphthalimide unit. This molecular assembly has been polymerized using a palladium cross-coupling reaction with two different linkers, 1,1,1,2,2,2-hexabutyldistannane and (4,8-bis((2-ethylhexyl)oxy)benzo[1,2-*b*:4,5-*b*′]dithiophene-2,6-diyl)bis(trimethylstannane), to obtain the target polymers **NIP3T-poly** and **NIP3T-BDT-poly**, respectively. Both polymers exhibited an extended absorption up to 1000 nm and higher hole field-effect mobilities of up to 1.8 × 10^{-3} cm^2 V^{-1} s^{-1}, in comparison to the molecular assembly **NIP3T**, and precisely tuned energy levels that make them compatible with common p-type dopants like 2,3,5,6-tetrafluoro-7,7,8,8-tetracyanoquinodimethane (F_4TCNQ). After optimizing the doping level, we obtained a thermoelectric figure of merit up to zT = 0.02 for **NIP3T-BDT-poly**, comparable with benchmark F_4TCNQ-vapor doped polythiophenes.

Received 20th December 2024,
Accepted 18th February 2025

DOI: 10.1039/d4tc05383d

rsc.li/materials-c

Introduction

The quest for sustainable and efficient energy conversion technologies has spotlighted the field of organic thermoelectric materials for turning *low-temperature* waste heat into electrical power.[1–4] Among the various materials under investigation, organic π-conjugated polymers are attractive due to their natural abundance of carbon-based structures, tunable opto-electrochemical properties by chemical design, and intrinsic light weight, flexibility, and solution processability.[5–8] These optimal characteristics suggest that polymer-based organic semiconductors can be high-performing materials for developing low-cost and environmentally friendly technologies.[9–11] However, within the field of organic thermoelectrics, most of the research is still focused on the study of polythiophene-based cores, and thus, exploring novel chemical designs with alternative polymer backbones remains largely an untapped avenue with the potential to unlock higher efficiencies and new functionalities that may benefit thermoelectric applications.

In recent years, a vast number of organic semiconductors (OSCs) have been developed for their application in organic photovoltaics (OPVs),[12] organic light-emitting diodes (OLEDs),[13] and organic field-effect transistors (OFETs).[14,15] These kinds of molecular/polymeric assemblies are now being explored for thermoelectric applications due to their relatively low thermal conductivity (κ) in the pristine state,[16] tunable electronic properties by molecular design, and feasible doping strategies to enhance their thermoelectric performance,[17–20] benchmarked by the figure of merit $zT = S^2\sigma T/\kappa$, where S is the Seebeck coefficient, σ the electrical conductivity, and T is the absolute

[a] Department of Organic Chemistry, Complutense University of Madrid, Faculty of Chemistry, Madrid 28040, Spain. E-mail: segura@quim.ucm.es
[b] Chemical and Environmental Technology Department, Rey Juan Carlos University, Madrid 28933, Spain
[c] Institut de Ciència de Materials de Barcelona, ICMAB-CSIC, 08193 Bellaterra, Spain. E-mail: mcampoy@icmab.es
[d] POLYMAT, University of the Basque Country UPV/EHU Av. De Tolosa 72, 20018, Donostia-San Sebastián, Spain
[e] Department of Chemistry and Chemical Engineering, Chalmers University of Technology, 41296 Göteborg, Sweden

† Electronic supplementary information (ESI) available. See DOI: https://doi.org/10.1039/d4tc05383d

‡ Equal contribution.

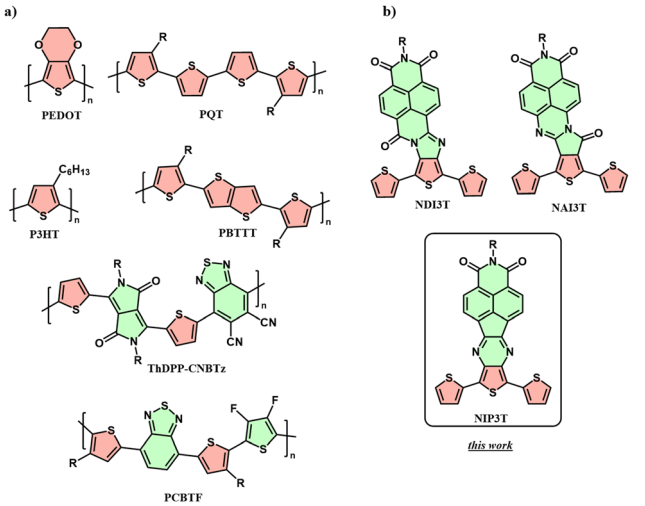

Chart 1 Chemical structures of (a) conventional conjugated polymers used in the field of thermoelectrics and (b) building blocks for polymers studied in this work.

temperature.[21] For instance, a recent n-type conjugated polymer based on a benzodifurandione moiety resulted in a breakthrough with impressive electrical conductivity[22,23] and stability of the doped state.[18,23]

Alternatively, most research on p-type OSCs is still focussed on the use of prototypical thiophene-based materials like poly(3,4-ethylenedioxythiophene) (PEDOT), poly(3,3′-dialkyl-quaterthiophene) (PQT), poly(3-hexylthiophene) (P3HT) and poly(2,5-bis(thiophen-2-yl)thieno[3,2-*b*]thiophene (PBTTT) (Chart 1a).

In the search for high-performance p-type organic polymers, a new synthetic strategy has recently been developed, in which the typical purely donor structure has been replaced by electroactive systems that alternate and combine strong donor units (mostly, thiophene derivatives) with strong acceptor units such as benzothiadiazole[24] (BT) or diketopyrrolopyrrole[25–27] (Chart 1a, PCBTF or ThDPP-CNBTz), where the most impressive electrical conductivities have been found by tuning the structural order (sometimes *via* glycolated sidechains) and anisotropy along the use of novel dopants[22,28–30]—with record power factors reaching 2.9 mW m^{-1} K^{-2}.[31] Within this context, a distinct and fresh approach that explores the synthesis of novel conjugated backbones for p-type thermoelectrics is still due. In this regard, D–A conjugated polymers can be envisaged as promising candidates because of their advantages in terms of high carrier mobilities, tunable properties, and versatile structures. To obtain a general overview of donor–acceptor polymeric systems, it is observed that most of them exhibit a similar chemical structure, where donor and acceptor units are alternated regularly or irregularly in the same horizontal direction, thus promoting effective conjugation between the different co-monomers.[32,33] However, this strategy often does not allow for the formation of planar systems, as some torsion is generated between the different electroactive backbones. Therefore, in the pursuit of planar and fully conjugated systems, with similar or enhanced optical and electrochemical properties, the application of new monomers could open new horizons in the development of novel polymeric semiconductors.

In the search for novel D–A conjugated polymers for thermoelectric applications, one exciting and unexplored strategy up to now is the use of oligothiophene-naphthalimide assemblies as electroactive moieties—chemical architectures which have been proven to be efficient in (opto)electronic technologies (Chart 1b).[34–37] These π-extended unit, in contrast to typical structures with linearly alternating donor and acceptor units, have strongly lateral electron-accepting units. This strategy allows maintaining a p-type structure by means of covalently connected terthiophenes, following the classical strategy, but with the novelty of having introduced strongly acceptor naphthalimide units in the central thiophenes trough a nitrogenated-based connector. The interest in using naphthalimide electron-acceptor units is three-fold: (i) it provides low-lying LUMO levels, (ii) the nitrogen atom of the imide allows the introduction of different alkyl chains for improving solubility, (iii) makes it feasible to modify the absorption and electrochemical properties through different conjugated linkers that tune their intramolecular charge transfer characteristics. In addition to these features, the synthesis of this nitrogen-doped connector offers a greener pathway for producing D–A electroactive monomers. This is largely due to its metal-free and mild temperature reaction conditions, as well as the inherent efficiency of the condensation reaction itself. Specifically, the reaction between the 1,2-diketone functionalities of the naphthalimide and the corresponding 1,2-diamine derivative effectively extends the π-conjugated system, as shown in Scheme S1 (ESI†).

This approach enables precise tuning of the optoelectronic properties in these electroactive building blocks,[36,38,39] where the LUMO is primarily located on the naphthalimide unit, while the HOMO resides in the oligothiophene segment, being totally segregated in this conjugated system. Herein, in search of planar and fully conjugated polymers with tuned HOMO/LUMO energy values, we designed and synthesized two novel electroactive oligomeric architectures[39] based on the oligothiophene-naphthalimide assembly of 2-(2-decyltetradecyl)-7,9-di(thiophen-2-yl)-1*H*-thieno[3″,4″:5′,6′]pyrazino[2′,3′:2,3]indeno[6,7,1-def]isoquinoline-1,3(2*H*)-dione (**NIP3T**), previously described in our group.[35,39] Using a palladium-catalyzed Stille cross-coupling reaction between **NIP3T-Br** and either 1,1,1,2,2,2-hexabutyldistannane (**1**) or (4,8-bis((2-ethylhexyl)oxy)benzo[1,2-*b*:4,5-*b*′]dithiophene-2,6-diyl)bis(trimethylstannane) **2** we obtained the target polymers **NIP3T-poly** and **NIP3T-BDT-poly**, respectively. Our findings indicate that both polymers exhibit (i) planar backbones, (ii) extended absorption up to 1000 nm, and (iii) HOMO/LUMO energy levels similar to other prototypical p-type semiconductors. After doping with $FeCl_3$ and further optimizing with an anion exchange methodology, as well as the doping level, we obtained *zT* values of 0.02. To the best of our knowledge, this is the first example of D–A electroactive polymers based on π-conjugated moieties with segregated HOMO/LUMO topology,[35,39,40] which can pave the way for new synthetic strategies toward a new family of thermoelectric materials.

Results and discussion

Polymer design, synthesis, and characterization

Firstly, the dibrominated D–A molecular assembly **NIP3T-Br** is obtained by condensation reaction between the corresponding naphthalimide 1,2-dione **NID** and 5″-dibromo-[2,2′:5′,2″-terthiophene]-3′,4′-diamine, previously described by our group (Scheme S1, ESI†).[39] Then, the synthesis of these new π-extended donor–acceptor polymers was carried out by Stille cross-coupling reaction between the dibrominated monomer **NIP3T-Br** and the corresponding distannylated linear derivatives **1** and **2** under solvothermal conditions, as it is depicted in Scheme 1, to obtain the target polymers **NIP3T-poly** and **NIP3T-BDT-poly**. All the tested conditions (Time, monomer loading and temperature) are summed in Table S1 (ESI†).

The molecular weight distribution of both polymers was characterized with gel permeation chromatography (GPC) at 150 °C with 1,2,4-trichlorobenzene as the eluent against polystyrene standards and matrix assisted laser desorption/ionization high-resolution mass spectrometry (MALDI-HRMS), which indicated the formation of low molecular weight oligomers[41] (Fig. S8–S11, ESI†). It is worth noting that the small polymer sizes were reproducibly obtained in the case of **NIP3T-poly**. In contrast, for the copolymer **NIP3T-BTD-poly**, more heterogeneous materials were observed based on MALDI-HRMS results. These differences in length and distributions will affect their corresponding optoelectrochemical properties, which are highly related to the effective conjugated length of the assemblies.[42–44] In addition, these polymers were also characterized by FT-IR, ^{1}H-NMR, and ^{13}C-CP-MAS NMR spectroscopy, all available in the ESI.† In the IR spectra, it is worth noticing that all of them present the corresponding signals ascribed to the naphthalimide units in both polymers at 1690 cm^{-1} (C═O stretching), as well as the pyrazine –C═N– signal at 1640 cm^{-1}, confirming the presence of the **NIP3T** unit[39,45] in all cases (Fig. S7, ESI†). In the NMR analyses of these fully conjugated, planar, and π-extended structures, the spatial arrangement of the alkyl chains may lead to aggregation phenomena and interactions, which could contribute to the broadening of ^{1}H-NMR signals. However, the main reason for this unresolved signals could be the lower solubility of these semiconductors, as well as the high dispersity of the obtained oligomers.[46,47] For that, in both **NIP3T-poly** and **NIP3T-BDT-poly** polymers, we observed poorly resolved signals ascribed to the naphthalimide units at 9.0–8.0 ppm, the thiophene' hydrogens between 7.6 and 7.0 ppm, the CH_2–N–protons from the imide and all the aliphatic alkyl chains below 4ppm. In the ^{13}C–CP–MAS NMR analyses, it is important to notice the presence of the imide (C═O) and the pyrazine (C═N) signals at 165 and 155 ppm, followed by all the C═C bonds of the structure and the carbon atoms directly connected to the oxygen (C–O) and nitrogen (C–N) atoms from the pendant alkyl chains between 85 and 40 ppm (Fig. S5 and S6, ESI†).

Thermogravimetric analysis (TGA, Fig. S12, ESI†) and differential scanning calorimetry (DSC, Fig. S13, ESI†) have also been carried out to study the thermal properties of these new polymers. These two polymers show an improvement in their degradation temperature (decomposition temperature of 5% and 6% at 300 °C for **NIP3T-poly** and **NIP3T-BTD-poly**) compared with the molecular analogue **NIP3T** (decomposition temperature of 10%), demonstrating that the functionalization of the alpha position of the terminal thiophene in the molecular analogue is directly associated with improved thermal characteristics and enhanced stability in the oligomers. However, the slightly variation in the TGA curves in the range of 30–300 °C could be associated with different factors such as the variable lengths of the oligomers,[42,48] the different nature/number of the cleavage pendant alkyl-chains[49,50] or possible traces of highly boiling point solvents. The DSC measurements of both **NIP3T-poly** and **NIP3T-BTD-poly** show no clear exothermic or endothermic processes at the range of 40 °C to 300 °C.[46]

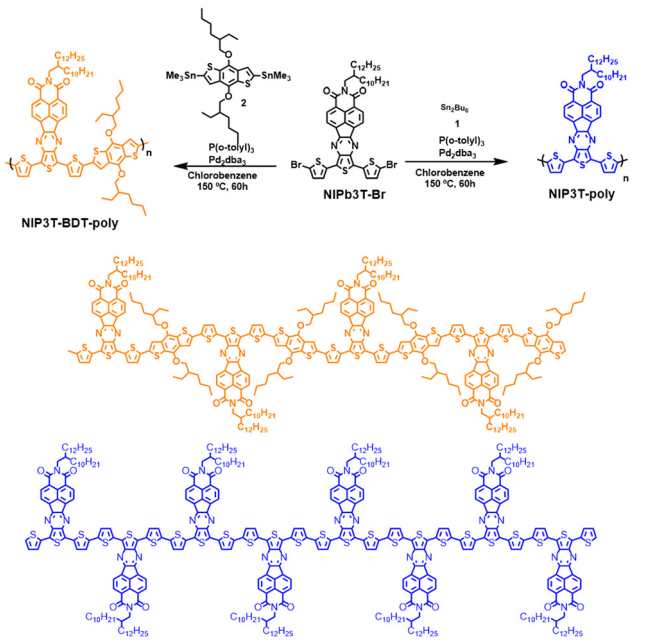

Scheme 1 Synthesis of **NIP3T-BDT-poly** and **NIP3T-poly** D–A–D polymers (top) and expanded chemical structures for these π-conjugated materials (bottom).

Optical and electrochemical properties

The solubility of **NIP3T-poly** and **NIP3T-BDT-poly** in chlorinated solvents, such as chlorobenzene or 1,2-dichlorobenzene, is moderate but still allows the characterization of their optical and electrochemical properties in solution using spectroscopic and electrochemical techniques. Tables 1 and 2 summarize the main values obtained for these polymers by UV-vis-NIR and cyclic voltammetry analyses, respectively.

Absorption spectroscopy. The UV-vis absorption spectra of **NIP3T-poly** and **NIP3T-BDT-poly** chlorobenzene fractions are compared in Fig. 1a. As we can see in their absorption profiles, these two polymers absorb across a broad range of wavelengths from 300 nm to 1000 nm, compared with the molecular analogue **NIP3T**, which only absorbs in the UV-vis region. These results, in addition to the concentration-dependent experiments

Table 1 UV-vis-NIR absorption measurements in chlorobenzene solutions

	λ_{max}^{sol} (nm)	λ_{onset}^{sol} (nm)	λ_{max}^{film} (nm)	$E_g^{opt\,a}$ (eV)
NIP3T	349	700	355	1.74
NIP3T-poly	355	1069	1070	1.16
NIP3T-BDT-poly	502	1026	1026	1.21

[a] Energy band gap derived from the low-energy absorption edge using the optical equation $E_g^{opt} = 1240/\lambda_{onset}$.

Table 2 Cyclic voltammetry recorded in chlorobenzene/$TBAPF_6$ (0.1 M) at a scan rate of 0.1 V s^{-1} using Pt as working and counter electrode, Ag/Ag^+ electrode as working electrode and Fc/Fc^+ as reference

	E_{oxI} (V)	E_{redI} (V)	$E_{HOMO}{}^a$ (eV)	$E_{LUMO}{}^b$ (eV)	$E_g^{elec\,c}$ (eV)
NIP3T	0.5	−1.4	−5.6	−3.7	1.9
NIP3T-poly	0.1	−1.4	−5.2	−3.7	1.5
NIP3T-BDT-poly	0.2	−1.4	−5.3	−3.7	1.6

[a] Estimated from $E_{HOMO} = -5.1\ eV - E_{oxI}$. [b] Estimated from $E_{LUMO} = -5.1\ eV - E_{redI}$. [c] Estimated from $E_g^{elec} = E_{HOMO} - E_{LUMO}$.

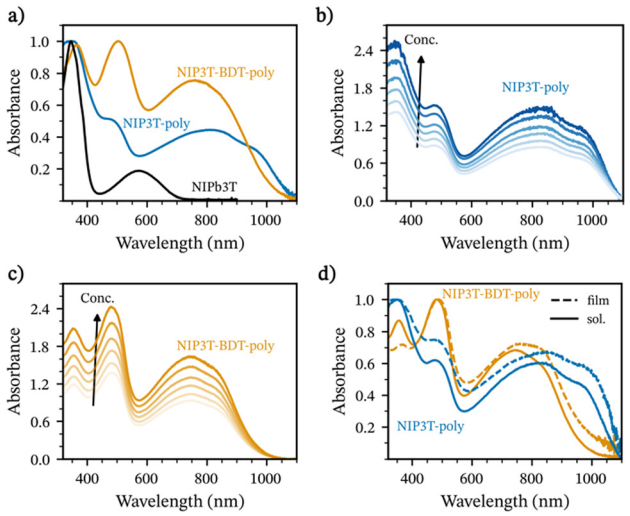

Fig. 1 (a) Normalized UV-vis-NIR spectra of chlorobenzene fractions of **NIP3T**, **NIP3T-poly** and **NIP3T-BDT-poly** in chlorobenzene, (b) and (c) concentration-dependent experiments for both polymers **NIP3T-poly** and **NIP3T-BDT-poly** respectively and (d) Normalized thin-film absorption spectra of these new oligothiophene-naphthalimide polymers. For (c) and (b), concentrations increase from 0.17 mg mL^{-1} to 0.30 mg mL^{-1}.

in chlorobenzene solutions (Fig. 1b and c) and spectroscopy of thin films (Fig. 1d), show that both **NIP3T-poly** and **NIP3T-BDT-poly**, present no differences between solution and the solid-state absorbance. This observation suggests that the conformation of the chains is similar in solution and in solid state, which may be because the material is aggregated in both solution and the solid state, even when they present an amorphous phase. The low solubility of the compounds, together with the lack of gas-to-solid shift and the behavior in the NMR analysis all support the pre-aggregation. The lack of strong diffraction peaks (*vide infra*) indicates that these aggregates are either small or have no long-range order.

The absorption onsets for these two polymers are red-shifted in comparison to the molecular analogue in solution, with values as high as 1026 nm and 1069 nm for **NIP3T-BDT-poly** and **NIP3T-poly** in contrast with the 700 nm value for the **NIP3T** molecular assembly. In addition, it is worth mentioning that the different absorption spectra for these polymers, which present similar D–A chemical structures, could be in part ascribed to the different length of the obtained polymers, phenomena also described in other works.[42,44] These wide-range absorption properties for these polymers let us include them in the narrow band-gap polymer family ($E_g^{opt} < 1.50$ eV), with E_g^{opt} values as narrow as 1.16 and 1.21 eV for **NIP3T-poly** and **NIP3T-BTD-poly**, respectively.

Cyclic voltammetry. Cyclic voltammetry (CV) measurements were carried out in an inert atmosphere to analyze the electronic properties of these novel polymers, and the data are summarized in Table 2. From the onset of the first reduction potentials obtained by CV in dry chlorobenzene (Fig. 2a), it is possible to estimate the lowest unoccupied molecular orbital (LUMO) energy levels of the oligothiophene-naphthalimide-based polymers **NIP3T-poly** and **NIP3T-BDT-poly** (Table 2). On the other hand, the highest occupied molecular orbitals (HOMO) energy level can also be estimated from the oxidation processes.

As depicted in Fig. 2b, the LUMO of both polymers and the molecular assembly remains practically unaltered because only slight variations in the reduction processes are observed when molecular and polymer assemblies are compared. However, oxidation processes were observed at 0.15 and 0.20 mV for **NIP3T-poly** and **NIP3T-BDT-poly**, while the oxidation wave of

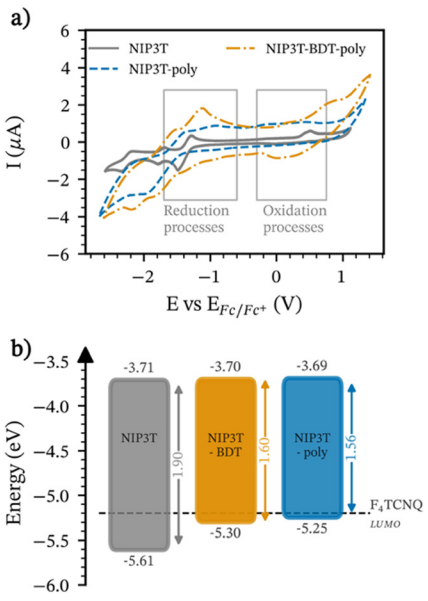

Fig. 2 (a) Cyclic voltammogram comparison between **NIP3T-poly** and **NIP3T-BDT-poly** organic conjugated polymers. (b) Molecular orbitals energy levels diagram of the studied π-conjugated polymers and the corresponding **NIP3T** molecular analogue in this work.

the **NIP3T** molecular analogue is found at 0.48 mV,[35,39] destabilizing the HOMO energy levels in the polymeric semiconductors. Based on these results, we can envisage oxidation of the polymer host with dopants like F_4TCNQ. Still, further chemical characterization would be necessary to discard the formation of charge-transfer complexes and side reactions leading to the polymer degradation, especially for **NIP3T-poly** which lacks a reversible oxidation peak (*cf.* Fig. 2a).[51,52]

In addition, it is worth noting that there is a good agreement between the optical and electrochemical properties in solution for both polymers, **NIP3T-poly** and **NIP3T-BDT-poly**, showing very similar absorption and redox tendency behaviors.

Electrical and thermoelectric characterization

Field-effect mobility. In order to extract the field-effect mobility of the polymers, **NIP3T-BDT-poly** and **NIP3T-poly** (thickness ~40 nm) were deposited on Si/SiOx substrates with interdigitated gold electrodes from a solution of chloroform: chlorobenzene (1 : 1) and annealed at temperatures of 150 °C and 180 °C. Fig. 3a and b shows the transfer characteristics (drain-source current (I_{DS}) *vs.* gate-source voltage (V_{GS}) at a fixed source-drain voltage (V_{DS})) for the materials studied in this work, and the corresponding output characteristics are shown in Fig. S14 of the ESI.† For both materials, we observe a decreasing drain-source current with positive gate voltage and thus conclude the material exhibits p-type characteristics. Additionally, we observed an improved performance for the devices with semiconducting polymer films annealed at 150 °C, probably due to differences in structural order. The highest hole mobility of **NIP3T-BDT-poly** is 1.8×10^{-3} cm^2 V^{-1} s^{-1}, about one order of magnitude higher than **NIP3T-poly** (1.6×10^{-4} cm^2 V^{-1} s^{-1}) and two-fold also in comparison with the recorded hole mobilities for the molecular analogue **NIP3T** (4.1×10^{-5} cm^2 V^{-1} s^{-1}) described previously.[35] We ascribe these observations to the lower solubility of **NIP3T-poly**, which often led to rough surfaces compared to **NIP3T-BDT-poly** and likely to a less interconnected network (See microscopy images in Fig. S15, ESI†).

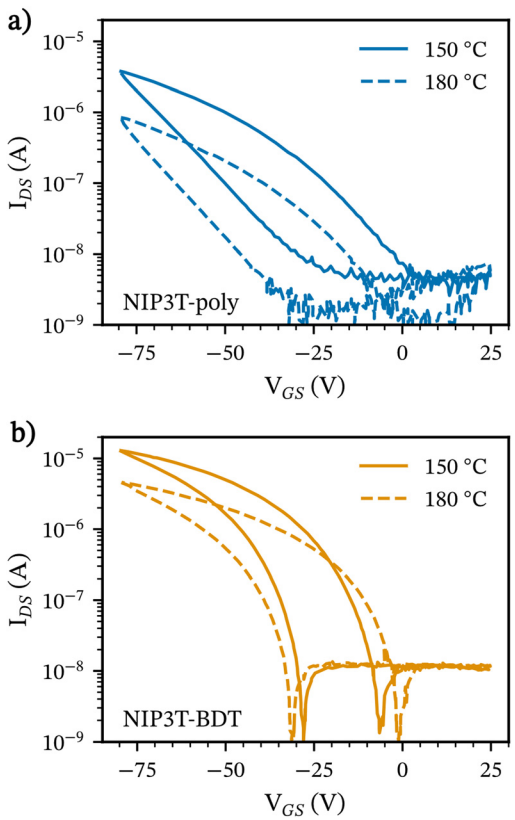

Fig. 3 Transfer characteristic curves for the OFETs based on (a) **NIP3T-poly** and (b) **NIP3T-BDT-poly** (V_{DS} = −80 V). Measurements were done on films thermally annealed at 150 °C and 180 °C.

Switch on voltages (V_{ON}) close to 0 V are observed in all devices; however, they exhibit significant hysteresis, which can be caused by charge trapping at the interface between the gate dielectric and the semiconductor. V_{ON} near 0 V means the traps do not significantly alter the balance of charges required to turn the device on. However, if those traps capture and release carriers in a dynamic manner, they can still cause significant hysteresis. Interestingly, **NIP3T-BDT-poly** based OFETs show a significant reduction in hysteresis when the polymer is annealed at 150 °C. Further solvent optimization should enable the fabrication of more uniform films, thereby reducing the number of defects at the semiconductor/dielectric interface, mitigating the observed hysteresis, and likely improving the device performance. Given previous observations, 150 °C was chosen as the annealing temperature for the following films throughout this work.

Absorption spectroscopy of the doped material. Two dopants were chosen to modulate the electronic properties of the polymer thin films (thickness ~70 nm): F_4TCNQ, given the compatible energy alignment with that of the polymers in this work, and $FeCl_3$, as it offers a larger operation window than other molecular dopants.[53] We also explored the anion exchange methodology, which uses $FeCl_3$ as the initial dopant and bis(trifluoromethane)sulfonimide (TFSI) as the exchanging anion.[54,55] Regardless, dopant concentration and solvent are comparable in all cases, and thus, differences in the doping level are likely due to the efficiency of different doping mechanisms and polymer:counterion interactions.

Fig. 4a and b shows the UV-vis-NIR spectra of the neat and oxidized polymers. Here, doping is confirmed by the characteristic bleaching of the neutral polymer absorption around 800 nm and the emergence of a polaron/bipolaron tail above 1000 nm.[56,57] For the case of F_4TCNQ-doped **NIP3T-poly**, we instead observe the presence of two bands centered at 1200 nm and 2300 nm that due to their shape and center tentatively ascribe to the presence of more localized polaron- and charge-transfer complex states.[58–62] Upon doping with $FeCl_3$, the center of P1 redshifts indicating an increase in the polaron delocalization length. This effect is more notorious on films of **NIP3T-BDT-poly** which can be ascribed to the prescence of delocalized polaron states.[60,61] Notably, doping seems less effective for the F_4TCNQ-doped films, particularly for **NIP3T-BDT-poly**. The latter is expected due to the deeper HOMO level

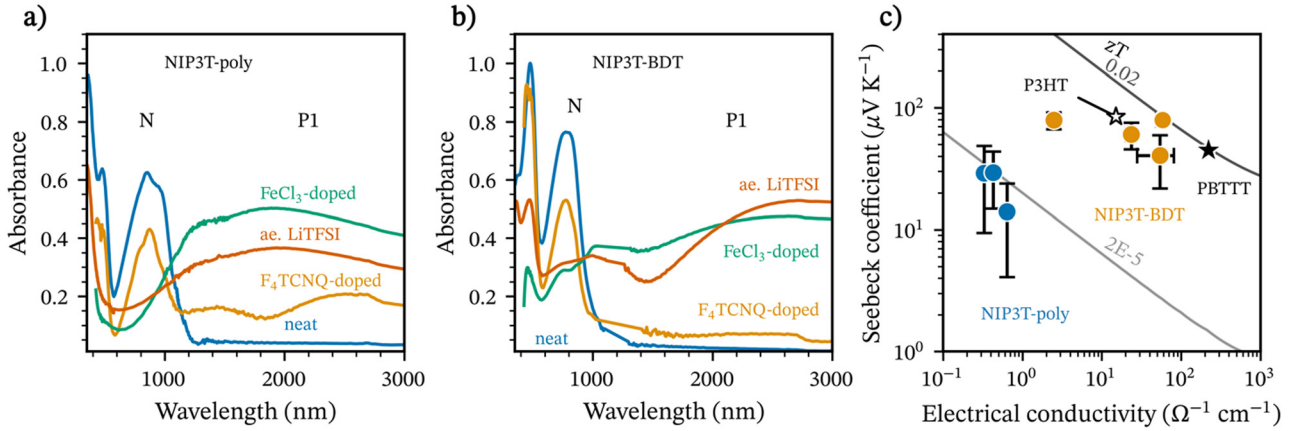

Fig. 4 UV-vis-NIR spectra of neat (a) **NIP3T-poly** and (b) **NIP3T-BDT** doped with doped with three different dopants (c) Seebeck coefficient as a function of the electrical conductivity for **NIP3T-poly** and **NIP3T-BDT** doped with three different dopants. Gray contour lines represent zT at different σ and S values using a 0.6 W m^{-1} K^{-1} determined with frequency domain thermoreflectance measurements. Error bars represent the standard deviation between 4 samples. The black and white stars represent values from the literature for F_4TCNQ-doped PBTTT and P3HT, respectively.

in the studied polymers (*vide supra*) compared to other benchmark materials like P3HT, which has a well-known interaction with the LUMO of F_4TCNQ.[63–67] Alternatively, Lewis-based dopants like $FeCl_3$ have a broad operation window and allow a higher doping level than F_4TCNQ in the case of both polymers. Noteworthy, under the studied blade-coating and spin-coating conditions, thin films were mostly transparent to the naked eye. On drop-casted films, visual cues between the neat and doped films were more obvious, as seen in Fig. S16 in ESI.†

Thermoelectric measurements. The electrical conductivity and Seebeck coefficients were measured on the same, approximately 2 × 2 cm^2 samples, and silver electrodes contacted the corners using a methodology and setup described in the literature.[68] A summary of the results of these measurements is shown in Fig. 4c, and more detailed values for each measurement are shown in Fig. S17 of the ESI.† The figure of merit was calculated using an out-of-plane thermal conductivity of 0.6 W m^{-1} K^{-1}. The chosen thermal conductivity corresponds to the mean value of measurements done for both materials using a frequency domain thermoreflectance methodology (see Fig. S17 in the ESI† and the experimental section). Here, thermoelectric performance of the optimized material (Fig. S19 and S20 of ESI†), as indicated by the figure of merit zT, is better for the materials that followed the anion exchange methodology, reaching zT values of 0.02 and 2 × 10^{-5} for **NIP3T-BDT-poly** and **NIP3T-poly**, respectively. Thus our best values while still below state-of-the-art thermoelectric materials are within the range of early experiments of solution co-processed F_4TCNQ-doped PBTTT and P3HT[69,70] Moreover the overall trend seems to agree well with the empirical power law observed by Glaudell *et al.*, $S \propto \sigma^{-1/4}$.[71]

Noteworthy is that the Seebeck coefficient and the electrical conductivity are higher for **NIP3T-BDT-poly** than for **NIP3T-poly**. These observations are partially expected: on one hand, the Seebeck coefficient is inversely proportional to the carrier concentration, and a first approximation between the relative intensity of the polaron bands compared to that of the neat material would indicate a lower doping level in **NIP3T-BDT-poly** than in **NIP3T-poly**.[72,73] Indeed, our spectral analysis and fitting suggest that for anion exchanged films, polaron mole ratio ranges between 0.07 for **NIP3T-BDT-poly** and 0.11 for **NIP3T-poly**, as seen in Fig. S18 (ESI†). Conversely, the electrical conductivity will scale with the carrier mobility (higher in **NIP3T-BDT-poly**) in the pristine material. At low doping levels we would expect a small increase in carrier mobility. Upon increasing the dopant content at levels common in organic thermoelectric applications, we can expect the dopant to disrupt structural order in the polymer network and thus induce a penalty on charge transport. Our experiments will later show that the structural order introduced by the dopant is lower in **NIP3T-BDT** than in **NIP3T-poly** and a relatively more ordered microstructure in the doped state, as indicated by GIWAXS analysis (*vide supra*). Overall, the performance of anion exchange doping on **NIP3T-BDT** is lower than state-of-the-art *anisotropic* samples[22] and that of isotropic polymers employing anion exchange methodologies.[54,55] At the current state, the presented work showcases values that are more comparable to '*solution co-processed*' isotropic samples of F_4TCNQ-doped P3HT, and F_4TCNQ-doped PBTTT reported in the literature.[70,71,74] Nonetheless, we envision that further optimization in the doping level, doping methodology and film fabrication protocol could improve the thermoelectric properties.

Structural characterization

We performed GIWAXS characterization to correlate the differences in thermoelectric performance with changes in the solid-state order of both neat and doped polymer films. Fig. 5 presents the 2D patterns and linecut integrations for films doped with $FeCl_3$, followed by an anion exchange with TFSI. The GIWAXS patterns reveal weak scattering features, indicating that the materials are predominantly amorphous. However, two rings are observed at q values of 2.5 (2.7) nm^{-1} for **NIP3T-BDT-poly** and **NIP3T-poly**, respectively. This indicates that at least some fractions of the materials have some degree of long-range order

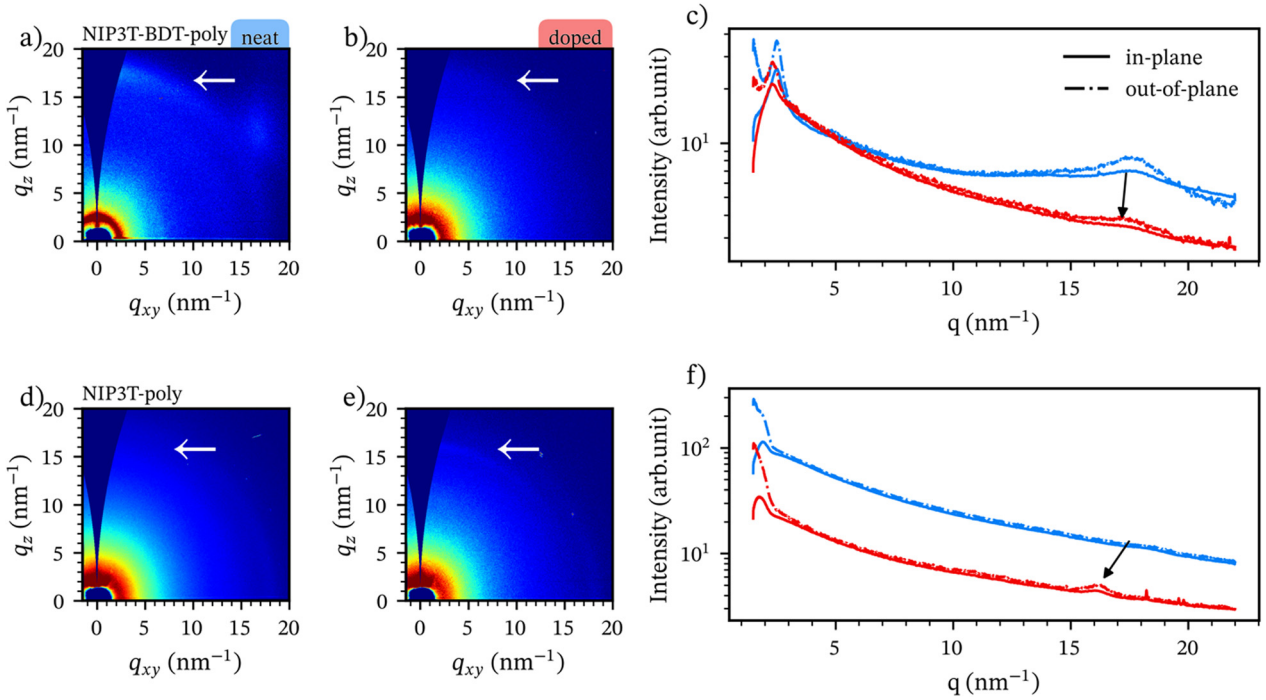

Fig. 5 2D GIWAXS patterns and linecuts for neat films and doped with $FeCl_3$ and subsequently exchanged using the anion exchange methodology. The panels "(a), (b) and (c)" correspond to **NIP3T-BDT-poly** whereas the panels "(d), (e) and (f)" correspond to **NIP3T-poly**. In the 2D patterns 15% of the background and top 10% was removed for clarity. Arrows have been added as guides to the eye for a weak scattering feature in the out-of-plane direction which decreases in intensity after doping for the **NIP3T-BDT-poly** and increases in intensity for the **NIP3T-poly**.

with similar lamellar spacings. In both cases, the scattering features point to a low degree of long-range order with an isotropic orientation.

In the neat material we highlight a scattering ring at 17.4 in the out-of-plane direction **NIP3T-BDT-poly** and *absent* in **NIP3T-poly**. We tentatively ascribe this observation to a better ordering in **NIP3T-BDT-poly** than **NIP3T-BDT-poly**, and thus agreeing with the better mobility and electrical conductivity measured in previous sections.

Upon doping, the (010) scattering peaks in **NIP3T-BDT-poly** attenuate considerably, indicating that doping introduces disorder in the material and thus agrees with the decrease in thermal conductivity observed in case of the neat material compared to the neat state[71,75] Strikingly, in case of **NIP3T-poly**, the (010) scattering peak increases slightly in intensity upon doping, which can indicate a partial dopant-induced ordering effect in this direction—an effect that has been observed for several other doped polymers and attributed to straightening of the polymer backbone upon charge delocalizaion.[76–80] Nonetheless, both materials remain highly amorphous.

Conclusions

In this work, we have designed, synthesized, and characterized two novel π-conjugated polymers with donor–acceptor architectures, named **NIP3T-poly** and **NIP3T-BDT-poly**, showcasing extended absorption up to 1000 nm, unipolar p-type electronic characteristics, and a thermoelectric figure of merit (zT) of up to 0.02. The demonstrated zT values, while still modest, compare favorably with other isotropic polythiophene derivatives that were initially the focus of the study in organic thermoelectrics. Of the two studied materials, doped-**NIP3T-BDT-poly** using the anion exchange methodology demonstrated superior thermoelectric performance, even though both materials have a low degree of long-range order before and after doping. This finding underscores the viability of these novel structures for their study and development in organic thermoelectrics. Additionally, it highlights that there is still room for improvement in film quality and structural order, which could be achieved by selecting other solvent systems.

Experimental section

Materials

Standard laboratory-grade solvents from Merck Aldrich and LabBox were used throughout. $FeCl_3$ and LiTFSI was purchased from Merck Aldrich. F_4TCNQ was purchased from Ossila.

Cyclic voltammetry

Cyclic voltammograms were recorded under an inert atmosphere in an electrochemical workstation at a scan rate of 100 mV s^{-1} at 20 °C using tetrabutylammonium hexafluorophosphate ($TBAPF_6$, 0.1 mol L^{-1}) as supporting electrolyte in chlorobenzene. Polymer-precoated platinum electrode, platinum–wire electrode, and Ag/Ag^+ electrode were used as

working-, auxiliary- and reference electrodes, respectively. Potentials were recorded *versus* Fc/Fc^+.

Thermal conductivity

Out-of-plane thermal diffusivity was measured using a frequency domain thermoreflectance methodology previously described in the literature.[81,82] The thermal conductivity is then calculated using a reference heat capacity (C_p) and density (ρ). To improve the sample's thermal sensitivity, a 60 nm Au layer is thermally evaporated onto the polymer surface. The method employs a pump laser at 405 nm to heat the film's surface locally and one at 532 nm as a probe. The pump laser is modulated to a harmonic waveform in the frequency range between 1 kHz and 100 kHz, which generates thermally induced harmonic oscillations of the reflectivity of the sample, thus leading to a modulation of the reflected power of the continuous wave probe laser. The phase lag between the pump and probe beams is then measured and fitted numerically along C_p and ρ.

Film fabrication

All thin films were fabricated under an ambient atmosphere except those used for OFET devices. Films with a thickness between 40 nm and 70 nm were blade-coated from mixtures of chloroform and chlorobenzene (5 : 95 vol) at concentrations of 4 mg mL^{-1} onto 75 mm × 25 mm glass slides precleaned with acetone and isopropanol. The deposition speed was changed from 30 mm s^{-1} to 50 mm s^{-1} depending on the thickness target while keeping a blade height of 150 μm and a temperature stage of 60 °C. For the electrical conductivity and Seebeck coefficient measurements, sets of four silver electrodes were thermally evaporated before film deposition. Alternatively, films for GIWAXS measurements and OFET devices were spin-coated in dynamic mode at 3000 rpm for 45 s onto Si/SiO_x (GIWAXS) and onto n-doped silicon substrates with a 230 nm SiO_2 layer, which featured interdigitated gold source and drain contacts with channel lengths of 2.5, 5, 10, and 20 μm (Fraunhofer IMPS). After deposition, the thin films were annealed following a 20 min thermal annealing at 150 °C in a N_2 glovebox. For OFET devices, annealing temperatures of 180 °C were also studied.

Doping

Sequential doping was performed for all samples. For F_4TCNQ- and $FeCl_3$-doped polymers, 200 μL of a 100 mM dopant solution in acetonitrile was placed onto the film's surface, left for 5 min, and then removed by tilting the polymer substrate. Alternatively, films doped using the anion exchange methodology were immersed in a solution of 5 mM $FeCl_3$ and 100 mM LiTFSI in acetonitrile at 40 °C for 5 minutes. In all cases, dopant excess was removed by spin-coating clean acetonitrile at a speed of 3000 rpm.

GIWAXS

Measurements were done at the NCD-SWEET beamline at the Alba synchrotron in Spain. Measurements were done in a gracing-incidence geometry with a beam energy of 12.4 keV, with the Pilatus detector at a distance of 21 cm and an incidence angle of 0.12°.

UV-vis-NIR spectroscopy

UV-vis-NIR absorption spectra were recorded using different setups. From 300 nm to 800 nm, the spectra were recorded with a Hitachi U3000 spectrophotometer, and from 800 to 3000 nm, they were recorded with a Bruker Vertex 70 FTIR spectrophotometer coupled to a Bruker Hyperion optical microscope.

Electrical conductivity and Seebeck coefficient

The electrical conductivity and Seebeck coefficient were measured on the same sample using a setup and methodology previously described in the literature.[68] All measurements were done under an ambient atmosphere.

Field effect mobility measurements

The electrical measurements were performed in a nitrogen-filled glovebox using a Keithley 2612A source meter and custom MATLAB software. The samples were connected using Everbeing tungsten probing tips. The devices were characterized by extracting the field-effect mobility (μ) in the saturation regime. μ was extracted from the fitting of the $I_{SD}{}^{1/2}$ *versus* V_{GS}.

Author contributions

Matías J. Alonso-Navarro: investigation, data curation, visualization, writing – original draft, writing – review & editing. Osnat Zapata-Arteaga: investigation, data curation, visualization, writing – original draft, writing – review & editing. Sergi Riera-Galindo: investigation, data curation, visualization, writing – review & editing. Jiali Guo: investigation, data curation, visualization. Aleksandr-Peredeventsv: investigation, data curation, visualization. Edgar Gutiérrez-Fernández: investigation, data curation, visualization. Juan Sebastián Reparaz: investigation, data curation, visualization. Mar Ramos: visualization, writing – review & editing. Christian Müller: visualization, writing – review & editing. Jaime Martín: visualization, writing – review & editing. Marta Mas-Torrent: conceptualization, investigation, visualization, supervision, writing – review & editing, funding acquisition, project administration. José L. Segura: conceptualization, investigation, visualization, supervision, writing – review & editing, funding acquisition, project administration. Mariano Campoy-Quiles.: conceptualization, investigation, visualization, supervision, writing – review & editing, funding acquisition, project administration.

Data availability

The data supporting this article have been included in the ESI.†

Conflicts of interest

There are no conflicts to declare.

Acknowledgements

This work was financially supported by the European Commission through the Marie Skłodowska-Curie project HORATES (GA-955837), MICINN (PID2022-138908NB-C33, PID2022-141393OB-I00 and TED2021-129886BC43), and through the ''Severo Ochoa'' Programme for Centers of Excellence in R&D (CEX2023-001263-S), and the UCM (INV.GR.00.1819.10759). MJAN gratefully acknowledges Universidad Rey Juan Carlos for his postdoctoral contract. S. R-G. is thankful to Marie Skłodowska Curie Cofund, Beatriu de Pinós Fellowship (AGAUR-2019 BP 00200) and Marie Sklodowska-Curie Actions (H2020-MSCA-IF-2020) for Grant Agreement No. 101025608, IDEAL. We thank Anders Mårtensson for help with SEC measurements, Dr Agustín Mihi (ICMAB-CSIC) for providing access to the Bruker IR spectrophotometry equipment, and Prof. Joaquim Puigdollers (UPC) for fruitful discussions.

Notes and references

1 M. Papapetrou, G. Kosmadakis, A. Cipollina, U. La Commare and G. Micale, *Appl. Therm. Eng.*, 2018, **138**, 207–216.
2 S. B. Riffat and X. Ma, *Appl. Therm. Eng.*, 2003, **23**, 913–935.
3 M. Ding, R. W. Flaig, H.-L. Jiang and O. M. Yaghi, *Chem. Soc. Rev.*, 2019, **48**, 2783–2828.
4 C. Forman, I. K. Muritala, R. Pardemann and B. Meyer, *Renewable Sustainable Energy Rev.*, 2016, **57**, 1568–1579.
5 X. Liu, C.-F. Liu, W.-Y. Lai and W. Huang, *Adv. Mater. Technol.*, 2020, **5**, 2000154.
6 A. Dessì, D. A. Chalkias, S. Bilancia, A. Sinicropi, M. Calamante, A. Mordini, A. Karavioti, E. Stathatos, L. Zani and G. Reginato, *Sustainable Energy Fuels*, 2021, **5**, 1171–1183.
7 D.-G. Wang, T. Qiu, W. Guo, Z. Liang, H. Tabassum, D. Xia and R. Zou, *Energy Environ. Sci.*, 2021, **14**, 688–728.
8 T. Qiu, Z. Liang, W. Guo, H. Tabassum, S. Gao and R. Zou, *ACS Energy Lett.*, 2020, **5**, 520–532.
9 F. Torricelli, I. Alessandri, E. Macchia, I. Vassalini, M. Maddaloni and L. Torsi, *Adv. Mater. Technol.*, 2022, **7**, 2100445.
10 A. Wadsworth, Z. Hamid, J. Kosco, N. Gasparini and I. McCulloch, *Adv. Mater.*, 2020, **32**, 2001763.
11 M. Ou, X. Wang, L. Yu, C. Liu, W. Tao, X. Ji and L. Mei, *Adv. Sci.*, 2021, **8**, 2001801.
12 G. Zhang, F. R. Lin, F. Qi, T. Heumüller, A. Distler, H.-J. Egelhaaf, N. Li, P. C. Y. Chow, C. J. Brabec, A. K. Y. Jen and H.-L. Yip, *Chem. Rev.*, 2022, **122**, 14180–14274.
13 P. Zuo, Y.-K. Qu, Q. Zheng, L.-S. Liao and Z.-Q. Jiang, *Mater. Chem. Front.*, 2023, **7**, 1760–1780.
14 G. S. Lee, H. Kwon, T. K. An and Y.-H. Kim, *Chem. Commun.*, 2023, **59**, 4995–5015.
15 K. Liu, B. Ouyang, X. Guo, Y. Guo and Y. Liu, *npj Flexible Electron.*, 2022, **6**, 1.
16 J. Liu, X. J. Wang, D. Y. Li, N. E. Coates, R. A. Segalman and D. G. Cahill, *Macromolecules*, 2015, **48**, 585–591.
17 L. Deng, Y. Liu, Y. Zhang, S. Wang and P. Gao, *Adv. Funct. Mater.*, 2023, **33**, 2210770.
18 R. Kroon, D. Kiefer, D. Stegerer, L. Yu, M. Sommer and C. Muller, *Adv. Mater.*, 2017, **29**, 1700930.
19 J. Liu, L. Qiu, G. Portale, M. Koopmans, G. ten Brink, J. C. Hummelen and L. J. A. Koster, *Adv. Mater.*, 2017, **29**, 1701641.
20 I. Petsagkourakis, S. Riera-Galindo, T.-P. Ruoko, X. Strakosas, E. Pavlopoulou, X. Liu, S. Braun, R. Kroon, N. Kim, S. Lienemann, V. Gueskine, G. Hadziioannou, M. Berggren, M. Fahlman, S. Fabiano, K. Tybrandt and X. Crispin, *Adv. Sci.*, 2023, **10**, 2206954.
21 M. Goel and M. Thelakkat, *Macromolecules*, 2020, **53**, 3632–3642.
22 A. Dash, S. Guchait, D. Scheunemann, V. Vijayakumar, N. Leclerc, M. Brinkmann and M. Kemerink, *Adv. Mater.*, 2024, **36**, 2311303.
23 H. Tang, Y. Liang, C. Liu, Z. Hu, Y. Deng, H. Guo, Z. Yu, A. Song, H. Zhao, D. Zhao, Y. Zhang, X. Guo, J. Pei, Y. Ma, Y. Cao and F. Huang, *Nature*, 2022, **611**, 271–277.
24 J.-F. Ding, G.-L. Chen, P.-H. Liu, K.-W. Tseng, W.-N. Wu, J.-M. Lin, S.-H. Tung, L. Wang and C.-L. Liu, *J. Mater. Chem. A*, 2024, **12**, 9806–9816.
25 J. Tang, J. Ji, R. Chen, Y. Yan, Y. Zhao and Z. Liang, *Adv. Sci.*, 2022, **9**, 2103646.
26 H. Zeng, M. Mohammed, V. Untilova, O. Boyron, N. Berton, P. Limelette, B. Schmaltz and M. Brinkmann, *Adv. Electron. Mater.*, 2021, **7**, 2000880.
27 Y. Gao, Y. Ke, T. Wang, Y. Shi, C. Wang, S. Ding, Y. Wang, Y. Deng, W. Hu and Y. Geng, *Angew. Chem., Int. Ed.*, 2024, **63**, e202402642.
28 D. Scheunemann, V. Vijayakumar, H. Zeng, P. Durand, N. Leclerc, M. Brinkmann and M. Kemerink, *Adv. Electron. Mater.*, 2020, **6**, 2000218.
29 E. Lim, A. M. Glaudell, R. Miller and M. L. Chabinyc, *Adv. Electron. Mater.*, 2019, **5**, 1800915.
30 L. Biniek, N. Leclerc, T. Heiser, R. Bechara and M. Brinkmann, *Macromolecules*, 2013, **46**, 4014–4023.
31 P. Durand, H. Zeng, T. Biskup, V. Vijayakumar, V. Untilova, C. Kiefer, B. Heinrich, L. Herrmann, M. Brinkmann and N. Leclerc, *Adv. Energy Mater.*, 2022, **12**, 2103049.
32 B. S. Desalegn, N. Bekri, F. G. Hone, D. M. Andoshe, W. Mammo, Z. Abdissa, G. Bosman and N. A. Tegegne, *Mater. Today Commun.*, 2021, **29**, 102803.
33 K. Dang Anh, P. L. dos Santos, M. Saeed, M. U. Chaudhry, I. H. Bechtold, A. Batycki, A. Drewniak, A. Szlapa-Kula and P. Ledwon, *Org. Electron.*, 2024, **129**, 107058.
34 R. P. Ortiz, H. Herrera, R. Blanco, H. Huang, A. Facchetti, T. J. Marks, Y. Zheng and J. L. Segura, *J. Am. Chem. Soc.*, 2010, **132**, 8440–8452.
35 R. P. Ortiz, H. Herrera, M. J. Mancheño, C. Seoane, J. L. Segura, P. M. Burrezo, J. Casado, J. T. L. Navarrete, A. Facchetti and T. J. Marks, *Chem. – Eur. J.*, 2013, **19**, 12458–12467.
36 A. de la Peña, I. Arrechea-Marcos, M. J. Mancheño, M. C. R. Delgado, J. T. L. Navarrete, J. L. Segura and R. P. Ortiz, *Chem. – Eur. J.*, 2016, **22**, 13643–13652.

37 M. J. Alonso-Navarro, E. Gala, M. M. Ramos, R. P. Ortiz and J. L. Segura, *Electron. Mater.*, 2021, **2**, 222–252.
38 M. J. Alonso-Navarro, A. Harbuzaru, R. González-Núñez, M. M. Ramos, J. L. Segura and R. P. Ortiz, *J. Mater. Chem. C*, 2023, **11**, 10852–10863.
39 M. J. Alonso-Navarro, A. Harbuzaru, P. de Echegaray, I. Arrechea-Marcos, A. Harillo-Baños, A. de la Peña, M. M. Ramos, J. T. L. Navarrete, M. Campoy-Quiles, R. P. Ortiz and J. L. Segura, *J. Mater. Chem. C*, 2020, **8**, 15277–15289.
40 A. Riaño, P. M. Burrezo, M. J. Mancheño, A. Timalsina, J. Smith, A. Facchetti, T. J. Marks, J. T. L. Navarrete, J. L. Segura, J. Casado and R. P. Ortiz, *J. Mater. Chem. C*, 2014, **2**, 6376–6386.
41 B. Zheng, J. Ni, S. Li, Y. Yue, J. Wang, J. Zhang, Y. Li and L. Huo, *Adv. Sci.*, 2022, **9**, 2105430.
42 R. Matsidik, H. Komber, M. Brinkmann, K. S. Schellhammer, F. Ortmann and M. Sommer, *J. Am. Chem. Soc.*, 2023, **145**, 8430–8444.
43 D. K. Tran, S. M. West, J. Guo, S. E. Chen, D. S. Ginger and S. A. Jenekhe, *J. Am. Chem. Soc.*, 2024, **146**, 1435–1446.
44 T. Mukhopadhyay, B. Puttaraju, P. Roy, J. Dasgupta, A. Meyer, A. Rudnick, S. Tscheuschner, F.-J. Kahle, A. Köhler and S. Patil, *Chem. – Eur. J.*, 2017, **23**, 13718–13723.
45 M. J. Alonso-Navarro, J. Barrio, S. Royuela, N. Karjule, M. M. Ramos, J. I. Martínez, M. Shalom and J. L. Segura, *RSC Adv.*, 2021, **11**, 2701–2705.
46 X. Li, J. Guo, L. Yang, M. Chao, L. Zheng, Z. Ma, Y. Hu, Y. Zhao, H. Chen and Y. Liu, *Front. Chem.*, 2019, **7**, 362.
47 X. Guo and M. D. Watson, *Macromolecules*, 2011, **44**, 6711–6716.
48 G. Zhang, M. Zhu, J. Guo, J. Ma, X. Wang, H. Lu and L. Qiu, *Org. Electron.*, 2014, **15**, 2608–2615.
49 J. Shanahan, J. Oh, S. Y. Son, S. Siddika, D. Pendleton, B. T. O'Connor and W. You, *Chem. Mater.*, 2023, **35**, 10139–10149.
50 S. Inoue, H. Minemawari, J. Tsutsumi, M. Chikamatsu, T. Yamada, S. Horiuchi, M. Tanaka, R. Kumai, M. Yoneya and T. Hasegawa, *Chem. Mater.*, 2015, **27**, 3809–3812.
51 A. F. Paterson, A. Savva, S. Wustoni, L. Tsetseris, B. D. Paulsen, H. Faber, A. H. Emwas, X. Chen, G. Nikiforidis, T. C. Hidalgo, M. Moser, I. P. Maria, J. Rivnay, I. McCulloch, T. D. Anthopoulos and S. Inal, *Nat. Commun.*, 2020, **11**, 1–11.
52 F. Ziaeimoghaddam and R. Arefinia, *Prog. Org. Coat.*, 2022, **170**, 106952.
53 A. D. Scaccabarozzi, A. Basu, F. Aniés, J. Liu, O. Zapata-Arteaga, R. Warren, Y. Firdaus, M. I. Nugraha, Y. Lin, M. Campoy-Quiles, N. Koch, C. Müller, L. Tsetseris, M. Heeney and T. D. Anthopoulos, *Chem. Rev.*, 2021, **4**, 4420–4492.
54 Y. Yamashita, J. Tsurumi, M. Ohno, R. Fujimoto, S. Kumagai, T. Kurosawa, T. Okamoto, J. Takeya and S. Watanabe, *Nature*, 2019, **572**, 634–638.
55 T. L. Murrey, M. A. Riley, G. Gonel, D. D. Antonio, L. Filardi, N. Shevchenko, M. Mascal and A. J. Moulé, *J. Phys. Chem. Lett.*, 2021, **12**, 1284–1289.
56 A. J. Moulé, G. Gonel, T. L. Murrey, R. Ghosh, J. Saska, N. E. Shevchenko, I. Denti, A. S. Fergerson, R. M. Talbot, N. L. Yacoub, M. Mascal, A. Salleo and F. C. Spano, *Adv. Electron. Mater.*, 2022, **8**, 2100888.
57 C. Wang, D. T. Duong, K. Vandewal, J. Rivnay and A. Salleo, *Phys. Rev. B: Condens. Matter Mater. Phys.*, 2015, **91**, 085205.
58 M. B. Qarai, R. Ghosh and F. C. Spano, *J. Phys. Chem. C*, 2021, **125**, 24487–24497.
59 M. Balooch Qarai, R. Ghosh, N. J. Hestand and F. C. Spano, *J. Phys. Chem. C*, 2023, **127**, 6414–6424.
60 R. Ghosh, A. R. Chew, J. Onorato, V. Pakhnyuk, C. K. Luscombe, A. Salleo and F. C. Spano, *J. Phys. Chem. C*, 2018, **122**, 18048–18060.
61 A. J. Moulé, G. Gonel, T. L. Murrey, R. Ghosh, J. Saska, N. E. Shevchenko, I. Denti, A. S. Fergerson, R. M. Talbot, N. L. Yacoub, M. Mascal, A. Salleo, F. C. Spano, A. J. Moulé, G. Gonel, A. S. Fergerson, R. M. Talbot, N. L. Yacoub, T. L. Murrey, R. Ghosh, F. C. Spano, J. Saska, N. E. Shevchenko, M. Mascal, I. Denti and A. Salleo, *Adv. Electron. Mater.*, 2022, **8**, 2100888.
62 I. E. Jacobs, C. Cendra, T. F. Harrelson, Z. I. Bedolla Valdez, R. Faller, A. Salleo and A. J. Moulé, *Mater. Horiz.*, 2018, **5**, 655–660.
63 H. Méndez, G. Heimel, S. Winkler, J. Frisch, A. Opitz, K. Sauer, B. Wegner, M. Oehzelt, C. Röthel, S. Duhm, D. Többens, N. Koch and I. Salzmann, *Nat. Commun.*, 2015, **6**, 8560.
64 J. Li, G. Zhang, D. M. Holm, I. E. Jacobs, B. Yin, P. Stroeve, M. Mascal and A. J. Moulé, *Chem. Mater.*, 2015, **27**, 5765–5774.
65 H. Hase, K. O'Neill, J. Frisch, A. Opitz, N. Koch and I. Salzmann, *J. Phys. Chem. C*, 2018, **122**, 25893–25899.
66 J. Fuzell, I. E. Jacobs, S. Ackling, T. F. Harrelson, D. M. Huang, D. Larsen and A. J. Moulé, *J. Phys. Chem. Lett.*, 2016, **7**, 4297–4303.
67 O. Zapata-Arteaga, B. Dörling, A. Perevedentsev, J. Martín, J. S. Reparaz and M. Campoy-Quiles, *Macromolecules*, 2020, **53**, 609–620.
68 B. Dörling, O. Zapata-Arteaga and M. Campoy-Quiles, *Rev. Sci. Instrum.*, 2020, **91**, 105111.
69 S. N. Patel, A. M. Glaudell, K. A. Peterson, E. M. Thomas, K. A. O'Hara, E. Lim and M. L. Chabinyc, *Sci. Adv.*, 2017, **3**, e1700434.
70 E. Lim, K. A. Peterson, G. M. Su and M. L. Chabinyc, *Chem. Mater.*, 2018, **30**, 998–1010.
71 A. M. Glaudell, J. E. Cochran, S. N. Patel and M. L. Chabinyc, *Adv. Energy Mater.*, 2015, **5**, 1401072.
72 G. Zuo, H. Abdalla and M. Kemerink, *Adv. Electron. Mater.*, 2019, **5**, 1800821.
73 D. Scheunemann and M. Kemerink, *Organic Flexible Electronics*, Elsevier, 2021, pp. 165–197.
74 S. N. Patel, A. M. Glaudell, K. A. Peterson, E. M. Thomas, K. A. O'Hara, E. Lim and M. L. Chabinyc, *Sci. Adv.*, 2017, **3**, e1700434.
75 O. Zapata-Arteaga, A. Perevedentsev, S. Marina, J. Martin, J. S. Reparaz and M. Campoy-Quiles, *ACS Energy Lett.*, 2020, **5**, 2972–2978.
76 P. Y. Yee, D. T. Scholes, B. J. Schwartz and S. H. Tolbert, *J. Phys. Chem. Lett.*, 2019, **10**, 4929–4934.

77 S. Hultmark, M. Craighero, S. Zokaei, D. Kim, E. Järsvall, F. Farooqi, S. Marina, R. Kroon, J. Martin, I. Zozoulenko and C. Müller, *J. Mater. Chem. C*, 2023, **11**, 8091–8099.
78 J. Guo, P. Chen, S. Yang, H. Wei, Y. Liu, J. Xia, C. Chen, H. Chen, S. Wang, W. Li and Y. Hu, *Small Methods*, 2024, 2400084.
79 B. X. Dong, Z. Liu, J. W. Onorato, T. Ma, J. Strzalka, P. Bennington, C. K. Luscombe, C. K. Ober, P. F. Nealey and S. N. Patel, *Adv. Funct. Mater.*, 2021, **31**, 2106991.
80 S. R. Jackson, G. W. Collins, R. L. Kingsford, P. W. Martin, J. N. Keller and C. G. Bischak, *J. Mater. Chem. C*, 2024, **12**, 9804–9813.
81 L. A. Pérez, K. Xu, M. R. Wagner, B. Dörling, A. Perevedentsev, A. R. Goñi, M. Campoy-Quiles, M. I. Alonso and J. S. Reparaz, *Rev. Sci. Instrum.*, 2022, **93**, 34902.
82 A. J. Schmidt, R. Cheaito and M. Chiesa, *Rev. Sci. Instrum.*, 2009, **80**, 094901.